SUPPLEMENTARY INFORMATION

Perfusion and Permeability MRI Predicts Future Cavernous Angioma Hemorrhage and Growth

Je Yeong Sone, BA, Nicholas Hobson, MSc, Abhinav Srinath, BA, Sharbel G. Romanos, BA, Ying Li, MD, Julián Carrión-Penagos, MD, Abdallah Shkoukani, MD, Agnieszka Stadnik, MSc, Kristina Piedad, RN BSN, Rhonda Lightle, BS, Thomas Moore, BS, Dorothy DeBiasse, BS, Dehua Bi, MSc, Robert Shenkar, PhD, Timothy Carroll, PhD, Yuan Ji, PhD, Romuald Girard, PhD, and Issam A. Awad, MD

SUPPLEMENTARY MATERIALS AND METHODS

Imaging Acquisition and Postprocessing

The imaging acquisition protocol of vascular permeability and perfusion (1) were performed on a 3.0-Tesla Philips Achieva system (1-5) using T_1-weighted dynamic contrast enhanced quantitative perfusion (DCEQP) magnetic resonance imaging (MRI) sequence following a previously published protocol (4,5), which included a 3D time-of-flight angiogram and 2D saturation recovery gradient recalled sequence. Five axial slices were acquired for each DCEQP scan.

The raw magnetic resonance signal was converted to gadolinium concentration using T_1 mapping, allowing for the arterial input function to be used alongside per-voxel signal changes in an established two-compartment model (1,2). Permeability values were then calculated using the Patlak method (6) and perfusion using the model-independent Tikhonov deconvolution method (2). The postprocessing pipeline was implemented on MATLAB (MathWorks, Natick, MA).

The segmentation of each cavernous angioma (CA) lesion was performed on the largest lesional diameter with axial T_2-weighted Turbo spin echo MRI scans as anatomical reference in ImageJ (LOCI, University of Wisconsin, WI) (3,7).

Calculation of Permeability and Perfusion Lesional Descriptors

The 13 respective permeability and perfusion descriptors calculated using built-in MATLAB functions included parameters derived from pixel-intensity histograms: coefficient of variation (CV), entropy, kurtosis, mean, median, skewness, and upper and lower terciles (**Supplementary Table 1**).

CA segmentation was used to calculate lesion area (mm^2). A custom MATLAB algorithm was used to calculate the four spatial clustering descriptors: high- and low-value cluster means and areas, respectively. First, high- and low-value cluster areas were calculated by generating binary masks via thresholding, in which all values were above or below at least 1 standard deviation (SD) from the mean. Then, the pixels were grouped into clusters using a connected-components routine. Finally, mean and area for the largest cluster for both high- and low-value clusters were calculated.

This panel of imaging descriptors maximized the diversity of lesional permeability and perfusion characteristics. CV, entropy, skewness, and kurtosis reflected heterogeneity within the lesion (8). Mean, median, and the upper and lower terciles represented central tendency of permeability and perfusion values. High- and low-value clusters indicated how the "extreme" values of permeability and perfusion were distributed spatially throughout the lesion, as loci of shear stress (9,10) and changes in hemodynamics (11) were associated with CAs (9) and intracranial hemorrhage.

Plasma Biomarker Assays

Blood Collection, Plasma isolation, and Storage

From the subset of 30 CA patients, standard clinical 10-mL heparinized Vacutainer tubes (BD Vacutainer, Becton, Dickinson and Company, Franklin Lakes, New Jersey, USA) were used to collect the blood samples. The assessment of biological compounds within heparinized blood plasma samples is in accordance with standard clinical practice and bio-assay kit manufacturer instructions (12). Only the biological compounds not affected by fasting state were assessed (13) because patients did not fast prior to clinical visits, which took place at various times throughout the day. Plasma was then isolated from the blood samples by centrifugation at 500 g at 4°C for 10

minutes (AllegraX-30R, Beckman Coulter, Brea, CA). The supernatant plasma was aliquoted into 200-μL samples in 1.7-mL microcentrifuge tubes and subsequently stored at -80°C.

Plasma protein biomarker assays

Eighteen plasma proteins were selected for immunoassay analysis in the previously published paper (14) based on systematic literature review of known mechanisms of CA disease and brain hemorrhage (15). These candidates included chemokine ligand 2 (CCL2/MCP1), soluble cluster of differentiation 14 (sCD14), C-reactive protein (CRP), interleukin-8 (IL-8/CXCL-8), interleukin-1 beta (IL-1β), interleukin-2 (IL-2), interleukin-6 (IL-6), interleukin-10 (IL-10), soluble matrix metalloproteinase-2 (MMP2) and -9 (MMP9), tumor necrosis factor alpha (TNFα), tumor necrosis factor receptor 1 (TNF-RI), soluble vascular endothelial growth factor (VEGF), soluble vascular cell adhesion protein 1 (sVCAM1), soluble roundabout guidance receptor 4 (sROBO4), soluble intercellular adhesion molecule 1 (sICAM1/CD54), interferon gamma (IFNγ), and soluble endoglin/CD105 (sENG). The candidate proteins were assessed using customized magnetic bead-based multiplex Luminex screening immunoassay kits (R&D Systems, Minneapolis, Minnesota, USA) (14). The immunoassays were measured with a Bio-Rad BioPlex-100 analyzer using the BioPlex Manager Software version 5.0 (Bio-Rad Laboratories, Hercules, California, USA) or the Luminex 200 System using the xPONENT Software (Luminex Corporation, Austin, Texas, USA). Plasma samples were loaded into parallel duplicate wells in each plate, from which their measurements were averaged. Fifty beads per region were collected for each well. The 5-parameter logistic regression analysis was utilized to estimate the sample concentration. Batch effects were identified using principal component analysis and corrected (14). All assessments were performed by the Flow Cytometry Core Facility at The University of Chicago.

Plasma protein biomarker equation

The Bayesian approach to model selection by minimizing the Akaike information criterion was utilized to develop the prognostic plasma CASH biomarker from the candidate proteins. The equation of the biomarker was calculated as the following:

$$\text{Biomarker} = -0.135*[\text{sCD14}] + 7.73*[\text{IL-1}\beta] - 0.775*[\text{VEGF}] + 0.658*[\text{sROBO4}].$$

The canonical scores of this prognostic plasma biomarker were used for the integrative analysis with the prognostic DCEQP imaging biomarker.

Statistical Analyses

Enrolled CA subjects who underwent DCEQP imaging versus those did not undergo imaging, as well as CA patients with versus without lesional bleed/growth among those who underwent DCEQP imaging were compared with independent samples t-test, Mann-Whitney U-test, χ^2-test, or Fisher's exact test using SPSS v22.0 (IBM, Armonk, NY). Post hoc analyses of χ^2-tests were conducted with comparisons of adjusted standardized residuals and Bonferroni corrections. Continuous variables were tested for normality with Shapiro-Wilk test. Prior to the Bayesian model selection process, collinearity within and between permeability and perfusion descriptors, respectively, was subsequently tested with Spearman ρ coefficients for exclusion from the final prognostic model (**Supplementary Figures 1–3**). The Youden method was utilized to calculate the optimal sensitivity and specificity of the receiver operating characteristic (ROC)

curves (16). The ROC curves were compared using the DeLong method (17), from which the *p*-values were false-discovery rate-corrected with the Benjamini and Hochberg method (18), using the R statistical framework (v4.1, R Foundation for Statistical Computing, https://www.r-project.org/). All *p*-values were considered statistically significant at $\alpha<0.05$.

SUPPLEMENTARY RESULTS

Comparison of Demographics between Patients Who Received Versus Did Not Receive DCEQP Imaging

Two-hundred and five CA patients underwent DCEQP imaging while 84 CA patients did not between July 2012 and December 2019 (**Supplementary Table 2**). A greater percentage of CA patients who underwent DCEQP imaging experienced lesional bleed/growth within a year after imaging ($p<0.05$). Higher percentages of CA patients scanned with DCEQP imaging were also younger and identified as white/Caucasian (all $p<0.05$). In contrast, greater proportions of CA patients who did not undergo DCEQP imaging were older (>50 years), identified as African Americans, and harbored multifocal unknown genotypes (all $p<0.05$). No significant differences in sex, sporadic/familial genotype, and brainstem lesion location were found between patients with and without DCEQP imaging.

Demographics of Patients with DCEQP Image Acquisition

Among the 205 CA subjects that underwent the DCEQP imaging, 20 experienced a lesional bleed/growth within a year after DCEQP imaging were enrolled (**Supplementary Table 3**). Greater proportions of CA patients with lesional bleed/growth were significantly younger and carried the *CCM3* genotype (both: $p<0.05$). No significant differences were observed between CA patients with versus without lesional bleed/growth within a year after imaging for sex ($p=0.63$), ethnicity/race ($p>0.99$), sporadic/familial phenotype ($p=0.058$), and whether the patient harbored a brainstem lesion ($p=0.58$) or a prior history of symptomatic hemorrhage ($p=0.13$).

CA Lesions with DCEQP Image Acquisition

Among CAs without lesional bleed/growth which were scanned with DCEQP imaging acquisition, one permeability and five perfusion scans were discarded due to postprocessing errors. Therefore, 721 CAs without bleed/growth had valid permeability scans, 717 with valid perfusion scans, and 716 with both.

SUPPLEMENTARY TABLES

Supplementary Table 1: The thirteen respective lesional permeability and perfusion imaging descriptors of cavernous angiomas generated from dynamic contrast-enhanced quantitative perfusion (DCEQP) maps.

DCEQP Descriptors	Descriptor Algorithm and/or Formula	Descriptor Definition
Coefficient of variation	$\frac{\sigma}{\mu}$	Standard deviation (σ) with respect to the mean (μ)
Entropy	$-\Sigma[p * \log_2(p)]$, in which p contains normalized histogram counts	Average level of randomness in the distribution of voxel values within the lesion
High-value cluster area & mean	Lesions masked by thresholding values at least 1 σ above mean; connected components selected using 'bwconncomp' MATLAB function	Largest cluster area of voxels at least 1 σ above mean of whole lesion, and the mean value of this cluster area
Kurtosis	$\frac{\mu_4}{\sigma^4}$	Extent of "tailedness" in which the distribution lies away from mean; μ_4: fourth central moment
Lesion area	$A = n * w * h$	Lesion area as selected in 2D axial image slice
Low-value cluster area & mean	Lesions masked by thresholding values at least1 below mean; connected components selected using 'bwconncomp' MATLAB function	Largest cluster area of voxels at least 1 σ below mean of whole lesion, and the mean value of this selected area
Mean	$\mu = \frac{1}{n}\sum_{i=1}^{n} x_i$	Average of lesion voxel values
Median	$\frac{x_{n/2} + x_{n/2+1}}{2}$	50th percentile value of lesional voxels
Skewness	$\frac{\mu_3}{\sigma^3}$	Extent of asymmetry within distribution about the mean; μ_3: third central moment
Terciles	$Upper = \frac{x_{\frac{2n}{3}} + x_{\frac{2n}{3+1}}}{2}$ $Lower = \frac{x_{\frac{n}{3}} + x_{\frac{n}{3+1}}}{2}$	Values grouped as above the 67th (upper) and below the 33rd percentile (lower)

Supplementary Table 2: Demographics of cavernous angioma (CA) patients who received dynamic contrast-enhanced quantitative perfusion (DCEQP) imaging in comparison to those who did not undergo DCEQP imaging.

Demographics	DCEQP (N=205)	No DCEQP (N=84)	*p*-value
CA with bleed/growth, N (%)	20 (9.8%)	2 (2.4%)	0.030
Age, Median (IQR)	40.1 (27.7–50.7)	50.9 (31.5–61.5)	0.001
Age Groups, N (%)			0.0001
< 30 years old	60 (29.3%)	14 (16.7%)	0.026
30 - 50 years old	91 (44.4%)	26 (31.0%)	0.035
> 50 years old	54 (26.3%)	44 (52.4%)	< 0.0001‡
Female, N (%)	130 (63.4%)	59 (70.2%)	0.28
Ethnicity/race, N (%) *			0.001†
African American	11 (5.4%)	16 (19.0%)	0.0003‡
Ashkenazi Jewish	3 (1.5%)	4 (4.8%)	0.099
Asian	6 (2.9%)	4 (4.8%)	0.44
Hispanic of Mexican descent	5 (2.5%)	4 (4.8%)	0.31
Hispanic of other descent	2 (1.0%)	1 (1.2%)	0.87
White/Caucasian	171 (83.8%)	55 (65.5%)	0.0006‡
Other	6 (2.9%)	0 (0.0%)	0.11
Sporadic, N (%)	115 (56.1%)	51 (60.7%)	0.51
Familial genotype, N (%)			0.022†
CCM1	29 (32.2%)	8 (24.2%)	0.39
CCM2	10 (11.1%)	4 (12.1%)	0.87
CCM3	26 (28.9%)	3 (9.1%)	0.022
Multifocal unknown	25 (27.8%)	18 (54.5%)	0.006‡
Brainstem lesion, N (%)	46 (22.4%)	14 (16.7%)	0.34

*One patient (0.5%) who received DCEQP imaging declined to provide information on ethnicity/race.
†Ethnicity/race and genotype were compared using Fisher's exact test.
‡These post hoc comparisons remained significant after respective Bonferroni corrections.
IQR: interquartile range.

Supplementary Table 3: Demographics of cavernous angioma (CA) patients with versus without lesional bleed/growth within a year after imaging.

Demographics	CA patients with bleed/growth (N=20)	CA patients with no bleed/growth (N=185)	*p*-value
Age, Mean ± SD (Range)	30.4±17.6 (5.2–59.6)	40.5±16.3 (4.4–79.6)	0.010
Age Groups, N (%)			0.028
< 30 years old	11 (55.0%)	49 (26.5%)	0.008‡
30 - 50 years old	6 (30.0%)	85 (45.9%)	0.17
> 50 years old	3 (15.0%)	51 (27.6%)	0.23
Female, N (%)	14 (70.0%)	116 (62.7%)	0.63
Ethnicity/race, N (%) *			> 0.99†
African American	1 (5.0%)	10 (5.4%)	
Ashkenazi Jewish	0 (0.0%)	3 (1.6%)	
Asian	0 (0.0%)	6 (3.3%)	
Hispanic of Mexican descent	0 (0.0%)	5 (2.7%)	
Hispanic of other descent	0 (0.0%)	2 (1.1%)	
White/Caucasian	19 (95.0%)	152 (82.6%)	
Other	0 (0.0%)	6 (3.3%)	
Sporadic, N (%)	7 (35.0%)	108 (58.4%)	0.058
Familial genotype, N (%)			0.034†
CCM1	4 (30.8%)	25 (32.5%)	0.90
CCM2	0 (0.0%)	10 (13.0%)	0.17
CCM3	8 (61.5%)	18 (23.4%)	0.005‡
Multifocal unknown	1 (7.7%)	24 (31.2%)	0.080
Brainstem lesion, N (%)	6 (30.0%)	42 (22.7%)	0.58†
Prior symptomatic hemorrhage, N (%)	3 (15.0%)	63 (34.1%)	0.13

*One patient without bleed/growth (0.5%) declined to provide information on ethnicity/race.
†Ethnicity/race, genotype, and brainstem lesion location were compared using Fisher's exact test.
‡These post hoc comparisons remained significant after respective Bonferroni corrections.
SD: standard deviation.

Supplementary Table 4: Covariates in the prognostic biomarker of cavernous angioma with bleed/growth within a year after imaging.

Variables	OR (95% CI)	*p*-value
Brainstem lesion location	4.6 (1.7–12.6)	0.003
Mean permeability	2.9 (1.5–5.9)	0.002
Low-perfusion cluster area	0.92 (0.87–0.98)	0.009
β_0	0.03	<0.0001

OR: odds ratio; CI: confidence interval; β_0: intercept of logistic regression equation.

SUPPLEMENTARY FIGURES

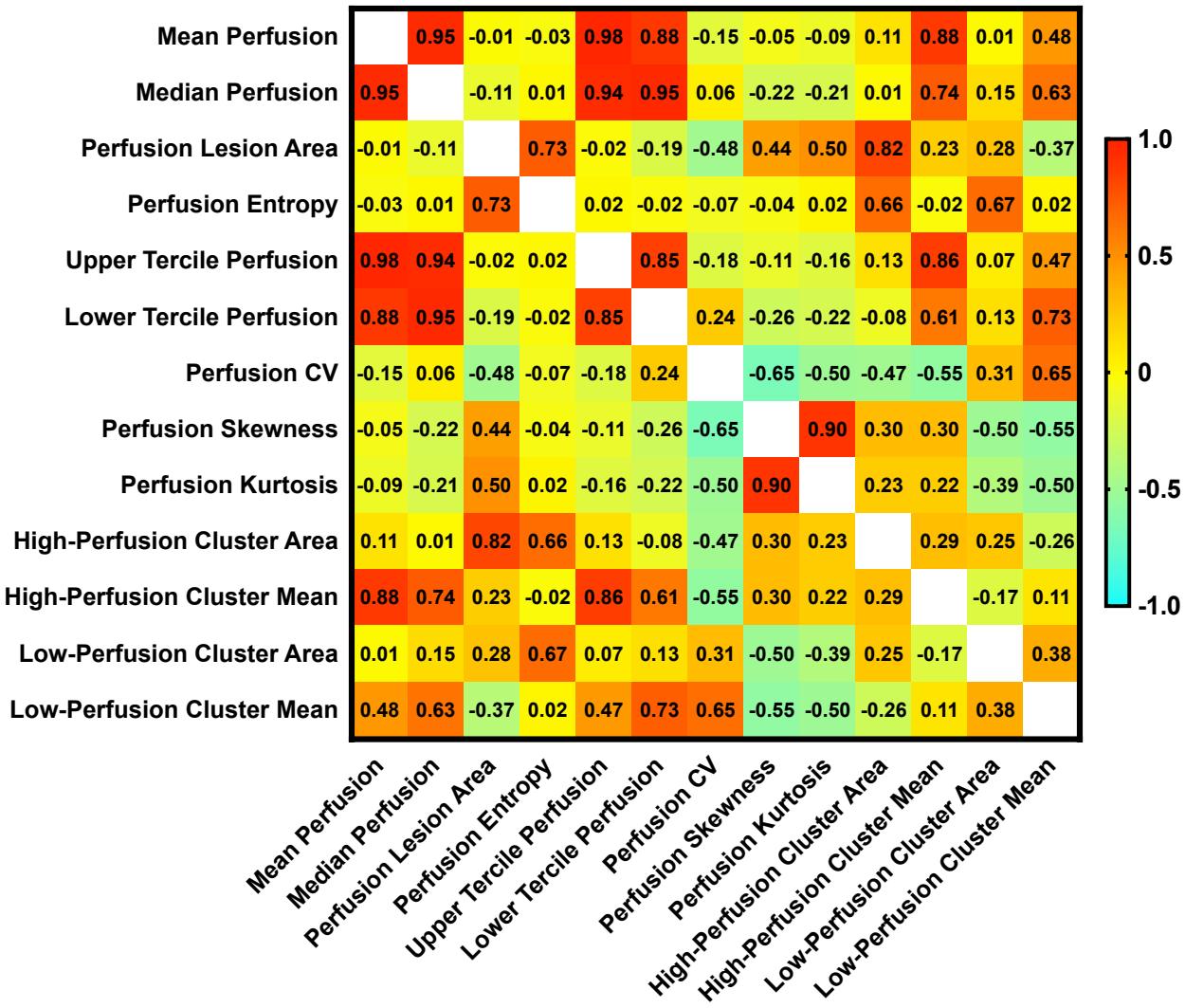

Supplementary Figure 1: Spearman's ρ correlations between perfusion descriptors of all cavernous angioma lesions with dynamic contrast-enhanced quantitative perfusion (DCEQP) imaging acquisition. Perfusion descriptors measured by DCEQP were tested for collinearity prior to Bayesian model selection (N=740). Highly collinear descriptors (ρ>0.50) were not included in the final model after minimizing the Bayesian information criterion. Spearman's ρ coefficients are shown in each cell. CV: coefficient of variation.

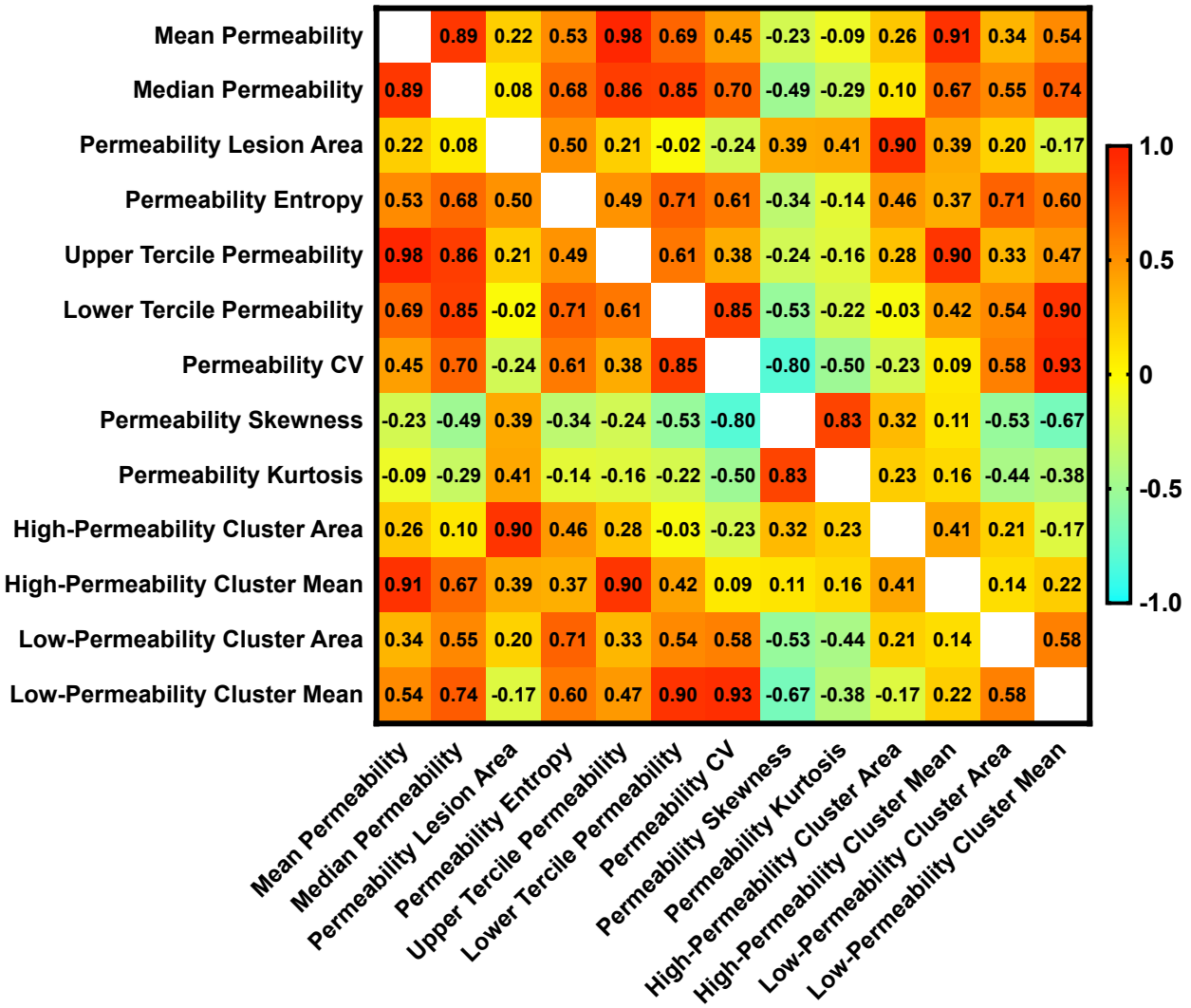

Supplementary Figure 2: Spearman's ρ correlations between permeability descriptors of all cavernous angioma lesions with dynamic contrast-enhanced quantitative perfusion (DCEQP) imaging acquisition. Permeability descriptors measured by DCEQP were tested for collinearity prior to Bayesian model selection (N=744). Descriptors that were highly collinear (ρ>0.50) were not included in the final model after minimizing the Bayesian information criterion. Spearman's ρ coefficients are shown in each cell. CV: coefficient of variation.

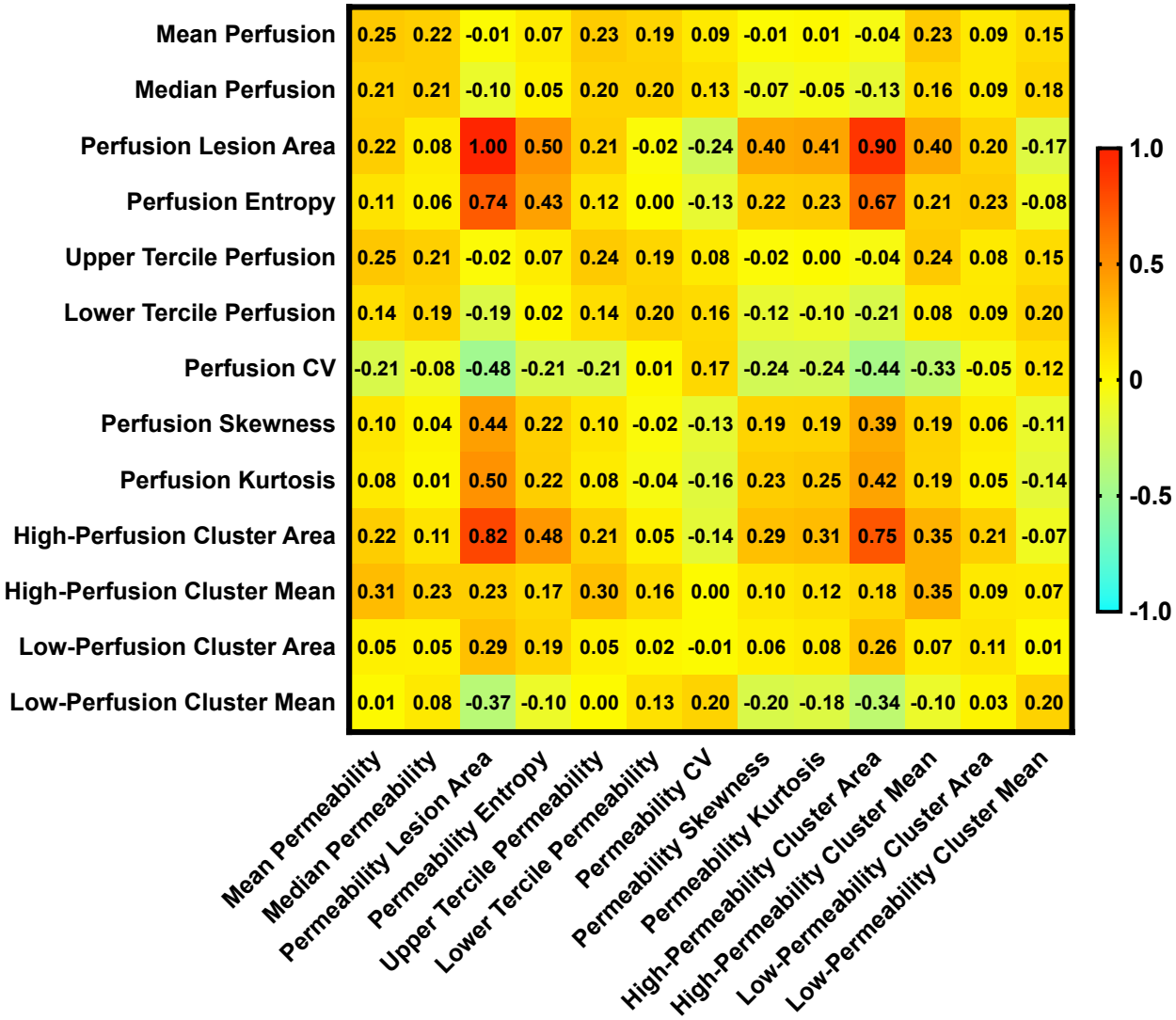

Supplementary Figure 3: Spearman's ρ correlations between perfusion and permeability descriptors of all cavernous angioma lesions with dynamic contrast-enhanced quantitative perfusion (DCEQP) imaging acquisition. Perfusion and permeability descriptors measured by DCEQP were tested for collinearity before the combined Bayesian model selection (N=739). Highly collinear descriptors (ρ>0.50) were not included in the final model after minimizing the Bayesian information criterion. Each cell shows the respective Spearman's ρ coefficient value. CV: coefficient of variation.

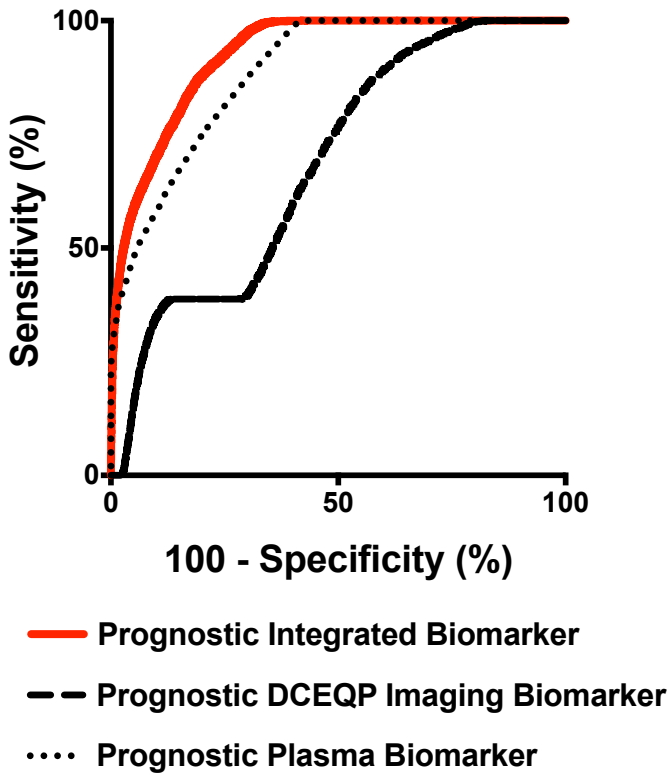

Supplementary Figure 4: Monte Carlo simulation of the integrated prognostic permeability, perfusion, and plasma protein biomarkers of cavernous angioma patients with bleed/growth within a year after imaging (N=5,000) versus those without lesional bleed/growth (N=24,999). The integrated permeability, perfusion, and plasma biomarker had 89% sensitivity and 79% specificity (area under the curve (AUC) [95% confidence interval (CI)]=93% [92–93%], $p<0.0001$), which performed significantly better than the imaging and plasma biomarker models individually (both: $p<0.0001$, FDR-corrected). Additionally, the plasma biomarker model outperformed the imaging model ($p<0.0001$, FDR-corrected). The combined permeability and perfusion imaging biomarker had 87% sensitivity and 43% specificity (AUC [95% CI]=68% [68–69%], $p<0.0001$). The plasma biomarker had 100% sensitivity and 59% specificity, AUC [95% CI]=89% [88–89%], $p<0.0001$). FDR: false discovery rate.

SUPPLEMENTARY REFERENCES

1. Larsson HB, Courivaud F, Rostrup E, Hansen AE. Measurement of brain perfusion, blood volume, and blood-brain barrier permeability, using dynamic contrast-enhanced T(1)-weighted MRI at 3 tesla. Magn Reson Med 2009;62:1270-1281.
2. Larsson HB, Hansen AE, Berg HK, Rostrup E, Haraldseth O. Dynamic contrast-enhanced quantitative perfusion measurement of the brain using T1-weighted MRI at 3T. J Magn Reson Imaging 2008;27:754-762.
3. Mikati AG, Khanna O, Zhang L, et al. Vascular permeability in cerebral cavernous malformations. J Cereb Blood Flow Metab 2015;35:1632-1639.
4. Girard R, Fam MD, Zeineddine HA, et al. Vascular permeability and iron deposition biomarkers in longitudinal follow-up of cerebral cavernous malformations. J Neurosurg 2017;127:102-110.
5. Hobson N, Polster SP, Cao Y, et al. Phantom validation of quantitative susceptibility and dynamic contrast-enhanced permeability MR sequences across instruments and sites. J Magn Reson Imaging 2019;51:1192-1199.
6. Patlak CS, Blasberg RG. Graphical evaluation of blood-to-brain transfer constants from multiple-time uptake data. Generalizations. J Cereb Blood Flow Metab 1985;5:584-590.
7. Tan H, Zhang L, Mikati AG, et al. Quantitative Susceptibility Mapping in Cerebral Cavernous Malformations: Clinical Correlations. AJNR Am J Neuroradiol 2016;37:1209-1215.
8. Zhang H, Li W, Hu F, Sun Y, Hu T, Tong T. MR texture analysis: potential imaging biomarker for predicting the chemotherapeutic response of patients with colorectal liver metastases. Abdom Radiol (NY) 2019;44:65-71.
9. Li J, Zhao Y, Coleman P, et al. Low fluid shear stress conditions contribute to activation of cerebral cavernous malformation signalling pathways. Biochim Biophys Acta Mol Basis Dis 2019;1865:165519. doi: 165510.161016/j.bbadis.162019.165507.165013.
10. Boyd AJ, Kuhn DC, Lozowy RJ, Kulbisky GP. Low wall shear stress predominates at sites of abdominal aortic aneurysm rupture. J Vasc Surg 2016;63:1613-1619.
11. Sharma A, Zipfel GJ, Hildebolt C, Derdeyn CP. Hemodynamic effects of developmental venous anomalies with and without cavernous malformations. AJNR Am J Neuroradiol 2013;34:1746-1751.
12. Zhou X, Fragala MS, McElhaney JE, Kuchel GA. Conceptual and methodological issues relevant to cytokine and inflammatory marker measurements in clinical research. Curr Opin Clin Nutr Metab Care 2010;13:541-547.
13. Langsted A, Freiberg JJ, Nordestgaard BG. Fasting and nonfasting lipid levels: influence of normal food intake on lipids, lipoproteins, apolipoproteins, and cardiovascular risk prediction. Circulation 2008;118:2047-2056.
14. Girard R, Zeineddine HA, Koskimaki J, et al. Plasma biomarkers of inflammation and angiogenesis predict cerebral cavernous malformation symptomatic hemorrhage or lesional growth. Circ Res 2018;122:1716-1721.
15. Girard R, Zeineddine HA, Fam MD, et al. Plasma Biomarkers of Inflammation Reflect Seizures and Hemorrhagic Activity of Cerebral Cavernous Malformations. Transl Stroke Res 2018;9:34-43.
16. Youden WJ. Index for rating diagnostic tests. Cancer 1950;3:32-35.

17. DeLong ER, DeLong DM, Clarke-Pearson DL. Comparing the areas under two or more correlated receiver operating characteristic curves: a nonparametric approach. Biometrics 1988;44:837-845.
18. Benjamini Y, Hochberg Y. Controlling the False Discovery Rate: A Practical and Powerful Approach to Multiple Testing. Journal of the Royal Statistical Society Series B (Methodological) 1995;57:289-300.